This article has been accepted for publication in Monthly Notices of the Royal Astronomical Society©: 2020 The Authors. *Published by Oxford University Press on behalf of the Royal Astronomical Society. All rights reserved.*

Monthly Notices
of the
ROYAL ASTRONOMICAL SOCIETY

MNRAS **494,** 1229–1236 (2020)
Advance Access publication 2020 April 2

doi:10.1093/mnras/staa813

The Northern Cross fast radio burst project – I. Overview and pilot observations at 408 MHz

Nicola T. Locatelli,[1,2]★ Gianni Bernardi,[2,3,4] Germano Bianchi,[2] Riccardo Chiello,[5] Alessio Magro ,[6] Giovanni Naldi,[2] Maura Pilia,[7] Giuseppe Pupillo,[2] Alessandro Ridolfi,[7,8] Giancarlo Setti[1,2] and Franco Vazza [1,2]

[1] *Dipartimento di Fisica e Astronomia, Universitá di Bologna, Via Gobetti 93/2, I-40129 Bologna, Italy*
[2] *INAF – Istituto di Radio Astronomia, via Gobetti 101, I-40129 Bologna, Italy*
[3] *Department of Physics and Electronics, Rhodes University, PO Box 94, Grahamstown 6140, South Africa*
[4] *South African Radio Astronomy Observatory, Black River Park, 2 Fir Street, Observatory, Cape Town 7925, South Africa*
[5] *University of Oxford, Department of Physics, Denys Wilkinson Building, Oxford OX1 3RH, UK*
[6] *Institute of Space Sciences and Astronomy (ISSA), University of Malta, Msida MSD 2080, Malta*
[7] *INAF – Osservatorio Astronomico di Cagliari, via della Scienza 5, I-09047 Selargius (Cagliari), Italy*
[8] *Max-Planck-Institut fuer Radioastronomie, Auf dem Huegel 69, D-53121 Bonn, Germany*

Accepted 2020 March 17. Received 2020 March 6; in original form 2020 January 13

ABSTRACT

Fast radio bursts (FRBs) remain one of the most enigmatic astrophysical sources. Observations have significantly progressed over the last few years, due to the capabilities of new radio telescopes and the refurbishment of existing ones. Here, we describe the upgrade of the Northern Cross radio telescope, operating in the 400–416 MHz frequency band, with the ultimate goal of turning the array into a dedicated instrument to survey the sky for FRBs. We present test observations of the pulsar B0329+54 to characterize the system performance and forecast detectability. Observations with the system currently in place are still limited by modest sky coverage ($\sim$9.4 deg^2) and biased by smearing of high dispersion measure events within each frequency channels. In its final, upgraded configuration, however, the telescope will be able to carry out unbiased FRB surveys over a $\sim$350 deg^2 instantaneous field of view up to $z \sim 5$, with a (nearly constant) $\sim 760\,(\tau/\mathrm{ms})^{-0.5}$ mJy rms sensitivity.

Key words: instrumentation: interferometers – pulsars: general.

1 INTRODUCTION

Fast radio bursts (FRBs) are extremely bright (1–100 Jy), impulsive (0.1–10 ms) transient events dispersed by their propagation through an ionized plasma. Their excess of dispersion measure (DM) with respect to the Galactic contribution is nowadays accepted as a convincing evidence of their extragalactic origin, but, beyond this, little is still known about their nature and physics (for a review on the topic, see Cordes & Chatterjee 2019; Petroff, Hessels & Lorimer 2019). Almost 100 FRBs have been observed to date and only a handful of them appear to repeat (Spitler et al. 2016; CHIME/FRB Collaboration 2019b; Kumar et al. 2019; The CHIME/FRB Collaboration 2019). A few FRBs have been localized, confirming their extragalactic origin, and their host environments have been found fairly different (Chatterjee et al. 2017; Michilli et al. 2018; Ravi et al. 2019). This scenario seems to indicate that FRBs may not be a single class of events, and significant effort is nowadays undertaken to localize more bursts (Bailes et al. 2017; Bannister et al. 2019; Kocz et al. 2019).

Beyond localization, the detection of a larger number of FRBs is crucial to discriminate among possible different populations (Caleb et al. 2016; Keane 2018; Macquart & Ekers 2018; Niino 2018; James et al. 2019; Locatelli et al. 2019), their emission mechanism (Ghisellini 2017; Lyutikov 2017; Ghisellini & Locatelli 2018) and their astrophysical environment (see Platts et al. 2018 for an updated review). Moreover, a larger statistical sample is necessary in order to use FRBs as effective cosmological probes (McQuinn 2014; Akahori, Ryu & Gaensler 2016; Macquart 2018; Vazza et al. 2018; Hackstein et al. 2019; Ravi 2019).

Initially, FRBs were detected at GHz frequencies (Lorimer et al. 2007; Thornton et al. 2013; Burke-Spolaor & Bannister 2014; Spitler et al. 2014; Petroff et al. 2015; Bhandari et al. 2018; Patel et al. 2018; Shannon et al. 2018), but recent observations in the 400–800 MHz range have enormously increased the FRB statistics (e.g. Caleb et al. 2016; CHIME/FRB Collaboration 2018, 2019a) and placed increasingly better upper limits on their event rate (Sokolowski et al. 2018; Sanidas et al. 2019; ter Veen et al. 2019), showing the advantage of large field-of-view (FoV) observations.

★ E-mail: nicola.locatelli2@unibo.it

© 2020 The Author(s)
Published by Oxford University Press on behalf of the Royal Astronomical Society

In this paper, we describe the ongoing effort to turn the Northern Cross (NC) radio telescope into a dedicated FRB survey machine observing at 408 MHz. We describe the current status of the instrumentation and related observations, and the forecast for upcoming surveys. Due to the large FoV of the NC, we expect a detection rate orders of magnitude higher than surveys carried out at GHz frequencies, in particular for distant ($z > 2$) events. From our initial estimates we expect to achieve performances comparable to the CHIME/FRB experiment.

The paper is organized as follows: in Section 2 we describe the current instrument status and recent upgrade, in Section 3 we present test observations that characterize the system, in Section 4 we forecast the FRB detection with the NC, and we conclude in Section 5.

2 INSTRUMENT DESCRIPTION

The NC is a T-shaped radio interferometer operating at 408 MHz, located at the Medicina Radio Astronomical Station (Bologna, Italy). Its orthogonal arms are aligned along the North–South (NS) and East–west directions, respectively (Fig. 1). Historically, the NC was used to survey the sky, producing several catalogues of extragalactic radio sources (e.g. Colla et al. 1970; Ficarra, Grueff & Tomassetti 1997; Pedani & Grueff 1999).

The NS arm has 64 reflective cylinders, 7.5 × 23.5 m each, for a total collecting area $A_{\mathrm{NS}} = 11\,280$ m^2. However, as the antenna efficiency is ∼0.71 (Bolli et al. 2008), the effective area is reduced to $A_{\mathrm{NS,\,eff}} \simeq 8000$ m^2. Each cylinder focuses the incoming radiation on 64 dipoles placed on the focal line; cylinders are spaced 10 m apart, leading to a total arm length of 640 m. The East–west arm was not used in this work.

2.1 Antenna and analogue receiver upgrade

The NS arm is undergoing an upgrade of the antenna and receiving system (see Montebugnoli et al. 2009, for details). The focal line of 16 cylinders has been modified in order to group the signals of 16 dipoles together, providing four analogue signals per cylinder, i.e. 64 receiving inputs for the refurbished sector (Fig. 2). Each receiving input (hereafter only receiver) is connected to a front-end box, mounted on top of the focal line, hosting a low noise amplifier and an optical fibre transmitter (Perini 2009a). The amplified radio frequency (RF) signals are sent to the station building through analogue optical fibre links (Perini 2009b). The RF receiver includes the optical–electrical conversion, filtering, amplification, conditioning, and single down-conversion to the intermediate frequency (IF) of 30 MHz (Perini et al. 2009). The output power can be digitally attenuated up to 31.5 dB in steps of 0.5 dB. A splitter chain architecture is used to distribute the local oscillator (378 MHz), clock, and synchronization signals to the IF circuitry.

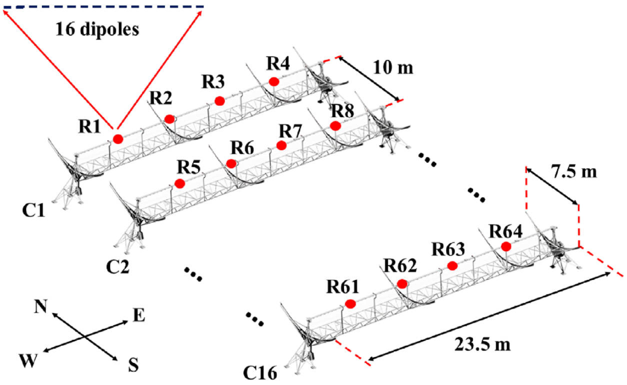

Figure 2. Scheme showing the refurbished section of the NS arm. The red circles indicate the position of the four receivers located on the focal line of each cylinder.

2.2 Digital backend

The digital acquisition and signal processing hardware is based on the Analog Digital Unit board (ADU; Naldi et al. 2017; Fig. 3), a digital platform developed for the Low Frequency Aperture Array (LFAA) component of the Square Kilometre Array. The ADU consists of 16 dual-input Analog to Digital Converters (ADCs) and two Field Programmable Gate Array (FPGA) devices, capable of digitizing and processing the broad-band (up to 400 MHz bandwidth) RF streams from 32 single polarization (or 16 dual polarization) antennas at an 800 MHz sampling rate. The 32 RF analogue inputs are digitized by 16 14-bits dual-input ADCs AD9680 that send the eight most significant bits to the XCKU040 FPGAs.

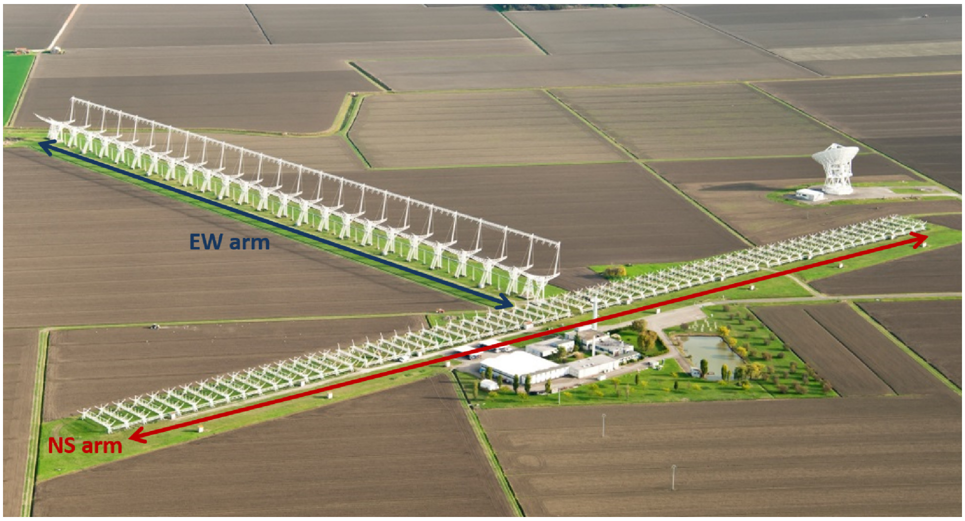

Figure 1. Aerial view of the Medicina Radio Astronomical Station. In the foreground, the NC with its two orthogonal arms.

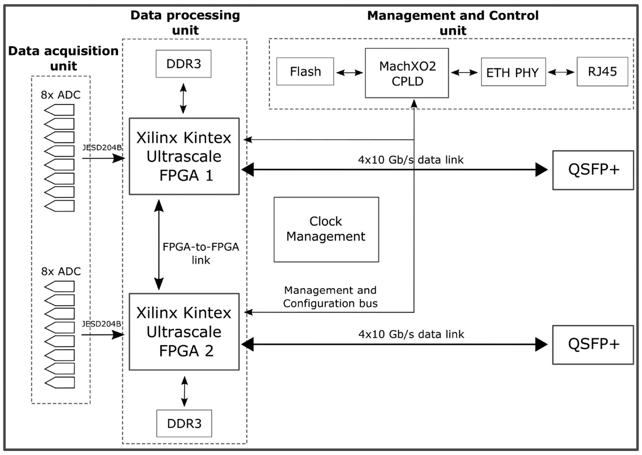

Figure 3. Block diagram showing the main functional parts of the ADU board.

Table 1. Characteristics of the current acquisition system.

N. of frequency channels	1024
Channel width	781.25 kHz
Time resolution	1.08 µs
Multibeam beamformer	
N. bits	16 complex
N. channels	384
N. beams	4
Max. time resolution	69.12 µs
Max. throughput	355.56 Mb s^{-1}
Single beam beamformer	
N. bits	16 complex
N. channels	21
Throughput	311.11 Mb s^{-1}

These samples are time stamped using a pulse-per-second signal with a reference high precision clock, and the ADU is synchronized to Coordinated Universal Time via the control interface.

The firmware design is highly modular, with a board specific I/O ring containing the interfaces to the physical peripherals and the control structure, and a core containing the signal processing chain (Comoretto et al. 2017). The board is controlled using an AXI4lite bridge to the 1 Gb Ethernet port, with each element seen as a memory mapped portion of the board address space. A map of this space is generated automatically at compile time and used by the control software to address each element by name (Magro et al. 2017).

Signal processing is performed on the FPGAs, with the resulting output data transferred to a processing server through a 40 Gb Ethernet connection.The signal processing chain includes:

(i) Correction for cable mismatch: Relative delays due to cable mismatch can be compensated for by applying a time-domain shift to each of the 24 IF inputs.

(ii) Channelization: Each of the 24 IF inputs are channelized into 512, 781 kHz-wide channels by an oversampled polyphase filterbank.

(iii) Correction of instrumental and geometric delays: Combined calibration and pointing coefficients are provided to the FPGAs. A calibration coefficient per antenna and per channel is required to correct for the receiver amplitude and phase response. Separate pointing coefficients are required for each generated beam, such that each beam can be pointed independently.

(iv) Frequency domain beamforming: The signal processing firmware can generate four simultaneous beams with a minimum integration time of ∼70 µs and one beam at 1.08 µs time integration. During this stage, the coefficients provided in the previous step are applied to each channelized data stream, thus simultaneously calibrating and pointing each beam.

The main features of the acquisition system are summarized in Table 1.

The ADU is managed using the monitoring and control software prototyped for the LFAA and uses the UniBoard Control Protocol for communication between the board and a compute server (Magro et al. 2017). The management software runs on the server and can read from and write to the FPGA memory address and other devices on the board. Management operations include: programming of the FPGAs; onboard device control; FPGA and ADC synchronization; network set-up; configuration of the signal processing chain; download of calibration and pointing coefficients for each beam; and instructions to broadcast control and data products. All processing on the ADU (i.e. from digitization to the transmission of beamformed data) is performed in real time.

The generated beams are transmitted from the ADU to the server over a 40 Gb link using a custom SPEAD protocol. A subset of the raw channelized data (the output of the firmware channelizer) can also be directly broadcast and used to generate calibration coefficients. Additional control data streams include transmission of raw antenna voltages and integrated spectra per antenna, both used to monitor the system performance.

Data streams are received at the compute server using the data acquisition system developed for the LFAA (Magro et al. 2019). The data acquisition system can process different simultaneous data streams concurrently. A ‘packet consumer’ is associated with each stream type, such that two specialized consumers are required: one to receive the fully sampled beam; and another to receive the raw channelized data. The channelized data streams are stored to disc using a simple binary format and are then correlated to generate calibration coefficients (see Section 3). The frequency channels of interest from the fully sampled beam are saved to disc using a modified version of the SigProc Filterbank file format (Lorimer 2011), where the complex voltages, rather than the power, are stored. This modification reduces the processing requirements (i.e. eliminates per-sample processing), resulting in the system being capable of writing data to disc in real time, and allows for custom offline software to convert the file to different file types such that no signal information is lost. For the tests described in this paper, custom filterbank files are converted to filterbank compatible files.

The system (front end and back end) described above is already a major upgrade over the pulsar back end used in the late 90s for pulsar searches and timing (D’Amico et al. 1996), however, we have already started to further optimize the system for FRB observations. In particularly, upcoming upgrades will include digitization at 700 MS s^{-1}, thus sampling the RF analogue band in the second Nyquist zone. The new design will implement a Digital Down Converter (DDC) that down converts the signal of interest to base band and filters out the image band that originates from the mixing operation. The sampling rate will be reduced by approximately two orders of magnitude and the channelizer modified accordingly, while maintaining the same oversampled polyphase filterbank structure. The beamformer will be redesigned in order to produce up to 20 independent beams, placed anywhere inside the single element FoV.

Table 2. Specifications of the NC test observations.

Central observing frequency	408 MHz
Analogue bandwidth	16 MHz
Total number of cylinders	6
Total number of receivers	24
Longest baseline (NS)	50 m
Receiver FoV	$\sim$38 deg ^{2}
Receiver FoV FWHM NS	5.9°
Receiver FoV FWHM East–west	6.4°

We are currently working on developing an online FRB search pipeline that performs the standard steps of dedispersion, candidate identification, and storage for further reprocessing (following a scheme similar to CHIME/FRB Collaboration 2018, for example), building on the HEIMDALL[1] publicly available code (e.g. Gajjar et al. 2018).

3 TEST OBSERVATIONS

We performed test observations in order to validate the system for FRB studies. As described in Section 2, the digital beamformer requires that the receiver signals are corrected for the corrupting effects that arise along the RF path. This calibration procedure is done through standard interferometric techniques where the channelized complex voltages υ from each receiver pair (i, j) are recorded and cross-correlated to form visibilities V_{ij}

$$V_{ij} = \langle \upsilon_i(t)\, \upsilon_j(t)^* \rangle_{\Delta t}, \tag{1}$$

where $\langle\rangle_{\Delta t}$ indicates the average over the integration time Δt and * is the complex conjugate. A software correlator is used to evaluate the right hand side of equation (1) by integrating the cross-products over $\Delta t = 1.13$ s, that is a trade-off between signal-to-noise ratio (SNR) and fringe smearing.

The instrumental corruptions can be described by complex receiver gains g

$$V^{\mathrm{o}}_{ij}(t, \nu) = g_i(t, \nu)\, g^*_j(t, \nu) V_{ij}(t, \nu), \tag{2}$$

where V^{o} are the observed visibilities, i.e. the visibilities that are corrupted by the instrumental response. The calibration procedure involves determining the instrumental gains g that can be solved for if the visibilities V_{ij} are known, i.e. through the observation of a calibration source. We observed Cas A, a standard calibrator for which we assumed a 4467 Jy flux density at 408 MHz (Perley & Butler 2017). Observations were carried out for $\sim$2 h in the single beam mode (details are reported in Table 2). Six cylinders are formed by a total of 24 receivers, leading to 276 independent baselines, most of which are redundant due to the regular configuration grid (see Fig. 2 for a reference scheme of the array used). Visibility data were edited and flagged, and calibration equations solved using two different minimization methods (Boonstra & van der Veen 2003), obtaining consistent solutions. Examples of visibilities compensated for the delay corresponding to the position of Cas A at the local meridian are shown in Fig. 4. The bottom panel clearly shows that, after calibration, the real part of the visibilities has maxima aligned in the desired direction, at hour angle $\omega = 0°$.

We used the derived antenna gains, combined with the geometric delay compensation coefficients, to beamform the six cylinder array towards the pulsar PSR B0329+54 (Cole & Pilkington 1968). PSR B0329+54 has a 714 ms period (Hobbs et al. 2004), a $S_{400} = 1500$ mJy flux density at 400 MHz (Lorimer et al. 1995) and a dispersion measure, DM = 26.7641 pc cm^{-3} (Hassall et al. 2012). It was observed for $\sim$20 min around transit.

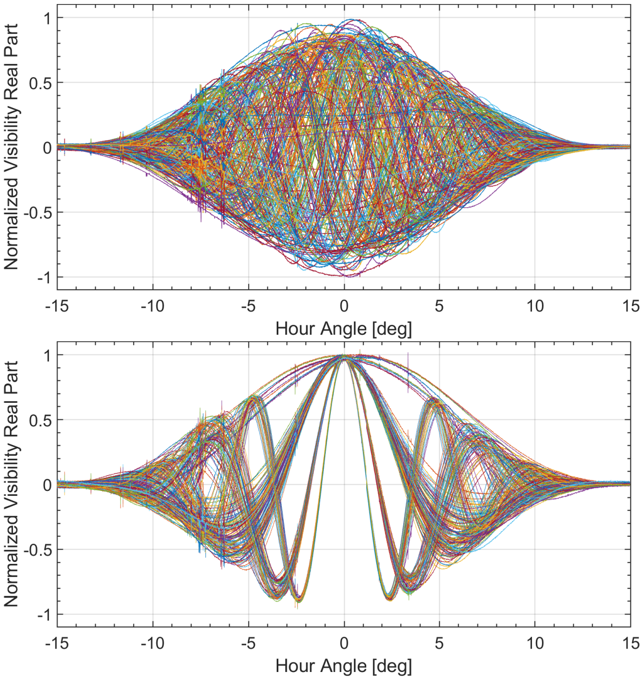

Figure 4. Real part of the complex visibilities corresponding to the transit of Cas A before (top panel) and after (bottom panel) calibration. Only the central channel at 407.6875 MHz is shown. Fringes show the main peak at transit ($\omega = 0°$) where they are phased, i.e. where the geometrical delay is compensated. Each colour corresponds to one of the 276 independent baselines. Fringe spacings are proportional to baseline lengths, therefore redundant visibilities appear grouped in subsets that have similar fringe frequencies.

We analysed 20 s-long observations using the standard DSPSR (van Straten & Bailes 2011), PSRCHIVE (Hotan, van Straten & Manchester 2004), and PRESTO (Ransom 2001; Ransom, Eikenberry & Middleditch 2002) suites for dedispersion, folding and radio frequency interference (RFI) excision. The time series was dedispersed and the single-pulse signal was folded over the integration. Our observations revealed a fairly benign RFI environment. A negligible fraction of the data were visually identified as corrupted and manually flagged.

Our observing band is partially (406–410 MHz) protected and reserved to radio astronomy and partially (400–406 and 410–416 MHz) is assigned to the Italian Minister of Economic Development, therefore we do not expect to have persistent but rather negligible RFI contamination as we found here. There is a regular RFI monitoring programme running at the Medicina station that shows a fairly low RFI occupancy. Interference signal mostly occur from atmospheric balloon probes but are confined to the low part of the band and limited at specific time intervals. Radio link transmissions are also generally short and sporadic. Nevertheless, we intend to implement more automatic RFI flagging strategies, ranging from simple amplitude clipping and standard deviation outliers, to machine learning classification (e.g. Pedregosa et al. 2012) and use spatially neighbouring beams to discriminate between man-made and sky signal (e.g. Bailes et al. 2017; CHIME/FRB Collaboration 2018).

---

[1] https://sourceforge.net/p/heimdall-astro/wiki/Use/

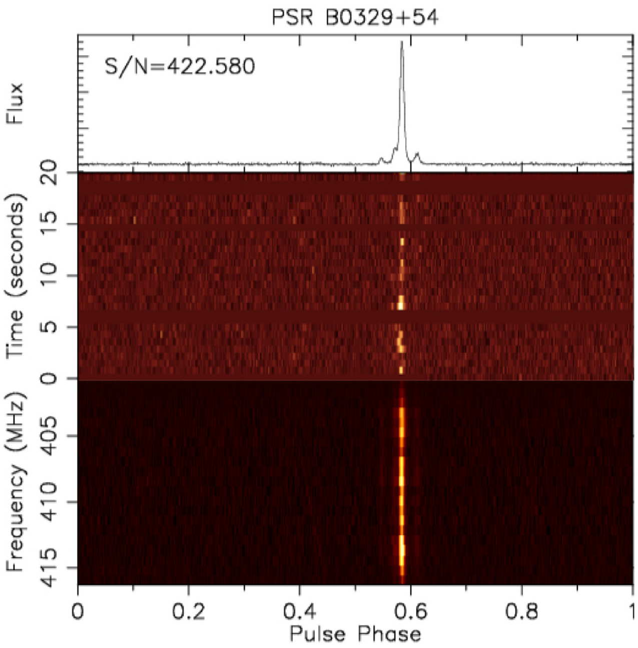

Figure 5. Observed profile of B0329+54. Bottom panel: intensity profile as a function of rotational phase and channel width, integrated over 20 s. We note a slight decrease at the band edges due to the sensitivity loss. Central panel: intensity profile as a function of a single-pulse time (~700 ms) over the 16 MHz bandwidth. The blanked horizontal bands represent time affected by RFI and therefore discarded. We note that no further flagging was needed. Top panel: pulse profile integrated over frequency and 20 s.

PSR B0329+54 was visible in each 20 s observation, and we used data taken closest to transit to estimate an SNR ~ 422 (Fig. 5), which, in turn, implies an rms noise $\sigma_6 = \frac{S_{400}}{\mathrm{SNR}} \sim 3.6$ mJy, where σ_6 indicates the sensitivity of the six cylinder array.

The derived sensitivity can be used to determine the system equivalent flux density (SEFD) of a single receiver, which is the quantity that we ultimately want to characterize. The receiver sensitivity σ is given by

$$\sigma = A\,\sigma_6, \tag{3}$$

where $A = 24$ is the ratio between the area corresponding to six cylinders and one receiver, respectively. The receiver SEFD is then given by the radiometer equation (for a similar approach, see Amiri et al. 2017)

$$\mathrm{SEFD} = \sigma\sqrt{N_\mathrm{p}\,B\,t} = A\sigma_6\sqrt{N_\mathrm{p}\,B\,t}, \tag{4}$$

where N_p is the number of polarizations measured, B the bandwidth, and t the observing time. In our case we have $N_\mathrm{p} = 1$, $B = 16$ MHz, $t = 20$ s, obtaining SEFD ~ 1530 Jy.

4 FRB SURVEY DESIGN

The system characterization allows us to forecast the FRB detectability with the NC. The telescope can already be used to observe known – i.e. repeating – FRBs, but, given its large FoV, it is best suited to carry out blind surveys to detect new FRBs.

The NC cylinders can be synchronously steered in declination by a common driveshaft that can be disabled, allowing each cylinder to be moved independently. The elevation range that can be observed without shadowing spans 45° from zenith, therefore $0° < \delta < 90°$ is the maximum observable declination range. Recalling that the receiver FoV is ~6° wide, 15 pointings are needed to cover the 90° declination interval. We therefore envisaged three different modes to observe FRBs with the NC:

(i) A pilot blind survey: the hardware and software upgrade described in Section 2 has been completed for eight cylinders that can, in turn, be split in two groups of four cylinders, each pointing 6° apart. With the current beamformer, each pointing can be tiled with four beams, each 1° × 1.6° wide, placed along the right ascension direction. Such survey will cover $A_\mathrm{FoV} \sim 9.4$ deg^2 instantaneously with a sensitivity σ_I

$$\sigma_I = \frac{\mathrm{SEFD}}{A_{16}\sqrt{B}} \sim 760\,(\tau/\mathrm{ms})^{-0.5}\ \mathrm{mJy}, \tag{5}$$

where $A_{16} = 16$, i.e. the number of receivers corresponding to four cylinders and τ is the observed time expressed in milliseconds (see also equation 6).

(ii) A blind survey that covers the widest possible area: once the whole NS arm is upgraded, the layout of the pilot blind survey can be extended to observe the whole declination range that can be accessed instantaneously, i.e. $0° < \delta < 90°$, covered by 15 pointings spaced 6° apart. Each pointing is observed with four cylinders, i.e. leading to the same sensitivity as per the survey I. The current system cannot take full advantage of the increased sky coverage as the four independent beams only cover ~ 10 per cent of the receiver FoV. For this survey we therefore considered that the improved multibeam and channelization capabilities anticipated in Section 2 are already deployed on all the 60 cylinders. If 20 independent beams are independently placed within the receiver FoV, the instantaneous sky coverage improves dramatically to $A_\mathrm{FoV} \sim 350$ deg^2. We will use this layout as our best case for FRB observations;

(i) Follow up of known (repeating) FRBs. Known sources can be followed for ~30 min as they transit through the receiver FoV. If 60 cylinders are beamformed together in a 4.5 arcmin × 1.6° beam, a $\sigma_{60} \sim 50\,(\tau/\mathrm{ms})^{-0.5}$ mJy sensitivity can be achieved.

A limitation of the current acquisition system is the relatively coarse frequency resolution that can lead to time smearing of high DM events. For a transient event of intrinsic duration t_i, equal or shorter than the sampling time Δt_b, the observed time τ is defined as (e.g. Amiri et al. 2017)

$$\tau = \sqrt{\Delta t_\mathrm{b}^2 + t_\mathrm{s}^2 + t_\mathrm{i}^2}, \tag{6}$$

where t_s is the scattering time and t_i is the intrinsic time duration of the event. If the signal propagates through an ionized plasma, it experiences an additional dispersion delay t_DM so that

$$\tilde{\tau} = \sqrt{\Delta t_\mathrm{b}^2 + t_\mathrm{s}^2 + t_\mathrm{i}^2 + t_\mathrm{DM}^2}, \tag{7}$$

where the dispersion smearing is (e.g. Burke-Spolaor & Bannister 2014)

$$t_\mathrm{DM} = 8.3\,\frac{\mathrm{DM}}{\left[\frac{\mathrm{pc}}{\mathrm{cm}^{-3}}\right]}\,\frac{\Delta\nu_\mathrm{ch}}{[\mathrm{MHz}]}\left(\frac{\nu}{[\mathrm{GHz}]}\right)^{-3}\ \mu\mathrm{s}, \tag{8}$$

where $\Delta\nu_\mathrm{ch}$ is the channel width and ν is the observing frequency. With the current system, an FRB with a DM = 647 pc cm^{-3} (the mean of the known FRB population to date, consistent with 665 pc cm^{-3} as estimated by Bhandari et al. 2018) would experience an intrachannel dispersion (smearing) $\tilde{\tau}$

$$\tilde{\tau} \simeq t_\mathrm{DM} \sim 62\,\mathrm{ms}, \tag{9}$$

Table 3. NC parameters for the two proposed surveys (see text for details): survey type; sampling time; channel width; instantaneous sky coverage; expected noise level (per millisecond).

Survey type	$\Delta t_{\rm b}$ (μs)	$\Delta\nu_{\rm ch}$ (kHz)	$A_{\rm FoV}$ (deg ^{2})	σ [mJy $(\tau/{\rm ms})^{-0.5}$]
I	70	781	9.4	760
II	276	3	350	760

that becomes 248 ms for the highest DM observed to date, 2596 pc cm^{-3} (Bhandari et al. 2018). A smaller channel width reduces the intrachannel smearing, normally implying an increase of the sampling time that, however, needs to remain sufficiently small to properly sample the burst duration. We quantified the impact of the intrachannel smearing for the surveys I and II by estimating the FRB event rate following Connor (2019). Table 3 summarizes the main specifications of both surveys, where, like we defined above, survey II already employs the finer channelization anticipated in Section 2.

Event rate estimates require the knowledge of the FRB cosmological distribution, their spectral index, their distribution in duration and their intrinsic luminosity. In particular, we adopted the following assumptions:

(i) a linear relation between the FRB dispersion measure and its redshift, i.e. DM $= 1000\,z$ pc cm^{-3} (Inoue & Ioka 2012; Dolag et al. 2015; Keane 2018; Zhang & Wang 2019);

(ii) a lognormal distribution for the FRB luminosity function at 1.4 GHz $L_{\rm GHz}$, peaking at 10^{33} erg s^{-1} and full width at half-maximum of 1.5;

(iii) a constant spectral index $\beta = 1.5$ for each event,[2] consistent with the average spectral index of known FRBs (Macquart et al. 2019). Although this assumption is likely incorrect, it only affects the rates observed at different frequencies and not the rates observed by the two surveys.

We assumed that the FRB cosmic evolution either follows the cosmic star formation rate (CSFR; Madau & Dickinson 2014), or a phenomenological formation rate (FRBFR; Locatelli et al. 2019). In their work, Locatelli et al. (2019) model the FRB cosmological evolution following the observed distribution of the events with DM $\lesssim 1000$ pc cm^{-3} (Macquart 2018; Shannon et al. 2018). In this model, the evolution is faster than the CSFR model and peaks at earlier redshifts. The cumulative event rate $\mathcal{R}_S$ above a given flux density threshold is shown in Fig. 6 (Fig. 7) for the CSFR (FRBFR) model. We also calculated the bias parameter b

$$b \equiv \frac{\mathcal{R}_S(\Delta\nu_{\rm ch})}{\mathcal{R}_S(\Delta\nu_{\rm ch} \rightarrow 0)}, \tag{10}$$

i.e. the ratio between a given rate and the ideal rate – i.e. the rate unaffected by intrachannel smearing. We note that FRBs have a noticeable spectral modulation at low frequencies (CHIME/FRB Collaboration 2018, 2019a,b), however, this effect is less prominent for the relatively narrow band of our observations, compared to wider bandwidth instruments.

We expect a significant loss of events due to intrachannel smearing for the survey I, with a magnitude that depends upon the chosen FRB model. In the CSFR case, there is essentially no event loss at the bright end of the cumulative event rate, whereas the completeness decreases to 17 per cent at the detection threshold. For the FRBFR case, the loss is already significant for bright events. The reason for this difference is due to the fact that low-redshift events have a higher DM in the FRBFR model than the CSFR one, leading to a higher intrachannel smearing.

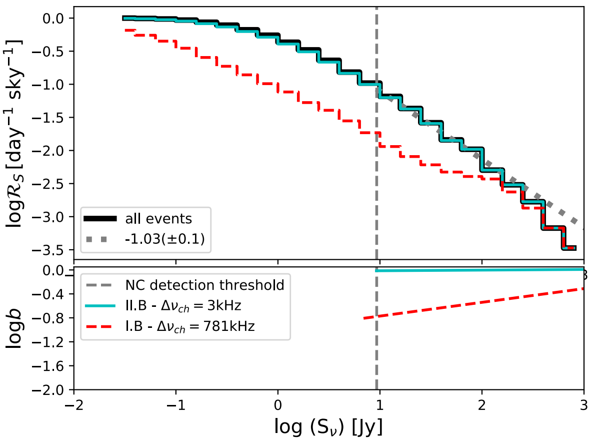

Figure 6. *Upper panel*: cumulative event rates $\mathcal{R}_S$ normalized to their relative peaks. The black solid line represents the theoretical prediction for the ideal case with no intrachannel smearing. The curve was fitted by a power law above the detection threshold. The best-fitting power law is plotted as a grey dotted line and its slope is reported in legend. The dashed red line and the solid cyan line show case I and II from Table 3, respectively. The cyan and black lines are virtually overlapping. The vertical dashed line represents the $10\sigma_I$ detection threshold – which is the same for both surveys. *Lower panel*: bias parameter b as a function of flux density (see text for details).

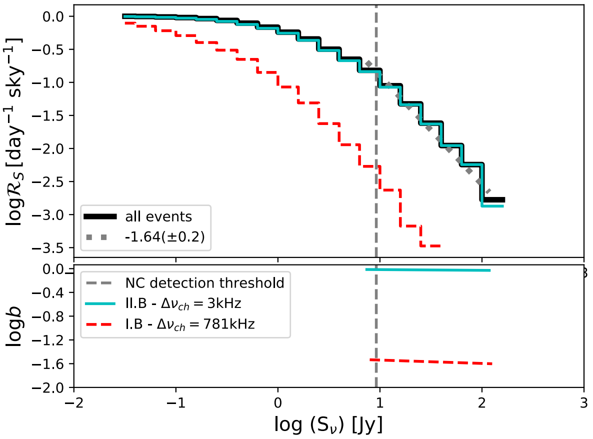

Figure 7. Same as Fig. 6, for the FRBFR model.

Survey II has, conversely, essentially no incompleteness (i.e. $b = 1$), regardless of the evolutionary model. This implies that the channelization adopted for survey II leads to an unbiased estimate of the true event rates. The bias introduced by intrachannel smearing is redshift dependent as more distant events generally entail larger dispersion measures. Fig. 8 displays two DM maps obtained from a cosmological simulation of the intergalactic medium (see Vazza et al. 2017, for the simulation details) that clearly show that larger DM values corresponds to larger cosmological volumes and therefore higher redshift events. The lower panel of Fig. 8 quantifies this effect using the linear DM–z relationship. For the survey I case, the dispersion of high-redshift FRBs leads to an SNR decrease of about one order of magnitude at $z \sim 1$, that is, only the brightest events are observable at high redshift. For survey II, conversely, the

---

[2] $S_\nu \propto \nu^{-\beta}$, where S_ν is the flux density at the frequency ν.

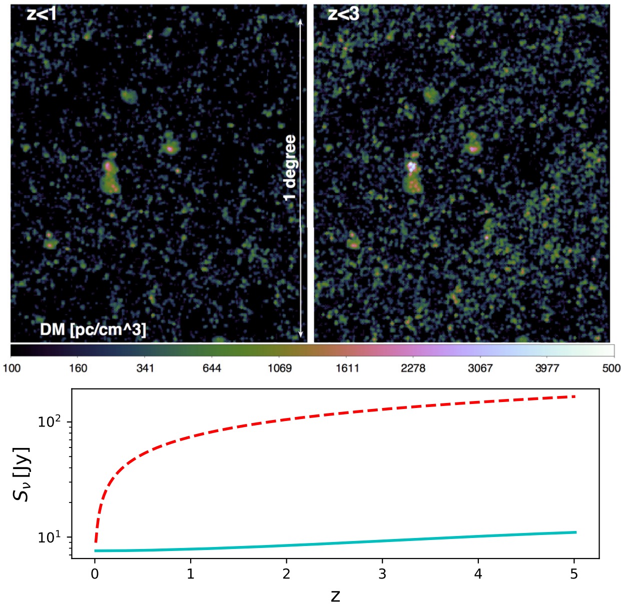

Figure 8. Upper panel: simulated dispersion measure map from a cosmological simulation, for a full light-cone with ≈1° aperture including the cosmic web up to $z = 1$ (left) or $z = 3$ (right). Lower panel: detection threshold as a function of the burst redshift, assuming a z–DM linear relation and a 1 ms burst duration, for survey I (dashed red line) and II (solid cyan line), respectively.

SNR only changes by $\sim$ 40 per cent up to $z = 5$. We finally assessed how much survey I and II constrain the FRB statistical properties. We assumed that the probability density function $\mathcal{P}$ of observing M events follows a Poissonian distribution (Vedantham et al. 2016; Amiri et al. 2017)

$$\mathcal{P}(M|N(\alpha)) = C\frac{N(\alpha)^M \mathrm{e}^{-N(\alpha)}}{M!}, \tag{11}$$

where N is the number of expected events and C is a normalization factor, chosen so that $\int \mathcal{P}(\alpha)\mathrm{d}\alpha = 1$. We assumed a power-law shape for the event rates N

$$N(\alpha) = 300\left(\frac{S_\nu}{1\,\mathrm{Jy}}\right)^{-\alpha} \times \mathrm{FoV} \times N_{\mathrm{day}}\ \ \mathrm{sky}^{-1}\,\mathrm{d}^{-1}, \tag{12}$$

where we used the event rate from CHIME/FRB Collaboration (2019b) as our pivotal value, that is, 300 events brighter than 1 Jy observed in the 400–600 MHz range.

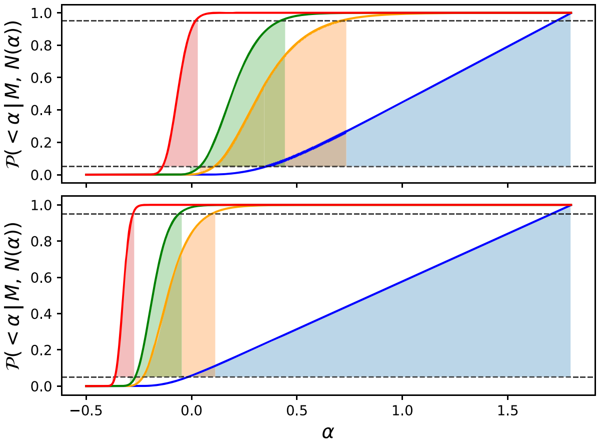

Figure 9. Constraints on the slope of the event rates for the survey II (top) and I (bottom panel), respectively. The probability is plotted as a function of 0 (blue), 1 (orange), 2 (green), and 10 (red) observed events over $N(\alpha)$ expected events for 30 observing days (720 h). Horizontal dashed lines show the 5 per cent and 95 per cent confidence levels, respectively.

The probability to find a slope smaller than α is thus given by the integral

$$P(<\alpha) = \int_{-\infty}^{\alpha} \mathcal{P}(M|N(\alpha'))\mathrm{d}\alpha', \tag{13}$$

while the probability of finding a slope greater than α is $1 - P(<\alpha)$. Constraints on the slope of the event rates are shown in Fig. 9 for survey I and II assuming a fiducial duration of 30 d. Due to its larger FoV, survey II will place better constraints on the event rate slope than survey I. A non-detection, in particular, will be able to rule out flat slopes, constraining $\alpha > 0.35$ at the 95 per cent confidence level.

Assuming $\alpha = 1$ (consistent with estimates at GHz frequencies; Vedantham et al. 2016; Amiri et al. 2017), we expect $\sim$ 40 $\mathrm{sky}^{-1}\,\mathrm{d}^{-1}$ events above the survey detection threshold, leading to one detection every 3 d for survey II. For survey I we expect to detect one burst in $\sim 112\,b^{-1}$ d, where the bias term incorporates the dependence upon the FRB evolutionary model due to DM smearing.

5 CONCLUSIONS

In this paper, we have described how the NC radio telescope is currently being equipped to carry out FRB surveys at 408 MHz. The current system uses a 16 MHz bandwidth divided in 21 781 kHz wide channels and consists of eight cylinders whose inputs can be combined into either a single beam or four independent ones with a sub-ms time sampling. Tests of the digital and software backend were carried out with six cylinders by observing the pulsar PSR B0329+54 from which the receiver SEFD = 1530 Jy was derived. Based on the derived SEFD, we presented forecasts for FRB searches using two different models of their cosmological evolution for two cases, one which uses the current system with eight cylinders (survey I) and an advanced one that uses 60 cylinders (survey II), for which we assumed the backend upgrades in terms of multi beam capabilities and finer channelization that are currently under development. For both cases, the rms sensitivity is $\sigma_I = 760\,(\tau/\mathrm{ms})^{-0.5}$ mJy, with an instantaneous sky coverage of 9.4 and 350 deg^2, respectively.

We found that the survey I is expected to detect one FRB every ∼112 d, although this rate suffers from smearing of high DM events and therefore depends upon the underlying FRB evolutionary model. Survey II is, conversely, immune from intrachannel smearing and is expected to yield one detection every 3 d, independently of the FRB model. Due to its large FoV, it is expected to probe FRBs up to $z \sim 5$ with an almost constant detection threshold. Based on the current low frequency event rates (CHIME/FRB Collaboration 2019b), survey II will be able to constrain the slope α of the event rate. In particular, in the case of no detections, a 720 h campaign will yield $\alpha > 0.35$ at the 95 per cent confidence level. Assuming a fiducial slope $\alpha = 1$, we expect ∼40 $\mathrm{sky}^{-1}\,\mathrm{d}^{-1}$ events above a $10\sigma_I$ detection threshold, that is, one detection every 3 d.

While the upgrade to carry out survey II is ongoing, the current system is being used to monitor repeating FRBs and improved localization capabilities are being considered by deploying receiving systems at 408 MHz at the other Italian radio astronomical stations.

ACKNOWLEDGEMENTS

We would like to thank an anonymous referee for useful comments. NTL and FV acknowledge financial support from the Horizon 2020 programme under the ERC Starting Grant 'MAGCOW', no. 714196. NTL also thanks Lorenzo Gamba, Liam Connor, and Manisha Caleb for helpful discussions. GB is in debt to Griffin Foster for his help in the early stages of the project. The ADU platform described in Section 2 is the result of a collaboration between the Italian Institute for Astrophysics (INAF), University of Oxford, University of Malta, Science and Technology Facility Council (STFC, UK) and was supported by industrial partners. The NC radio telescope is a facility of the University of Bologna operated under agreement by the Institute of Radio Astronomy of Bologna (INAF). The ENZO (enzo-project.org) simulation used for this work was produced on the Marconi-KNL Supercomputer at CINECA, under project no.INA17_C4A28 with FV as PI. We also acknowledge the usage of online storage tools kindly provided by the INAF Astronomical Archive (IA2) initiative (http://www.ia2.inaf.it). This research made use of ASTROPY,[3] a community-developed core PYTHON package for Astronomy (Astropy Collaboration 2013). AR gratefully acknowledges financial support by the research grant 'iPeska' (P.I. Andrea Possenti) funded under the INAF national call Prin-SKA/CTA approved with the Presidential Decree 70/2016.

REFERENCES

Akahori T., Ryu D., Gaensler B. M., 2016, ApJ, 824, 105
Amiri M. et al., 2017, ApJ, 844, 161
Astropy Collaboration, 2013, A&A, 558, A33
Bailes M. et al., 2017, Publ. Astron. Soc. Aust., 34, e045
Bannister K. W. et al., 2019, Science, 365, 565
Bhandari S. et al., 2018, MNRAS, 475, 1427
Bolli P., Perini F., Montebugnoli S., Pelosi G., Poppi S., 2008, IEEE Antennas Propag. Mag., 50, 58
Boonstra A. J., van der Veen A. J., 2003, IEEE Trans. Signal Process., 51, 25
Burke-Spolaor S., Bannister K. W., 2014, ApJ, 792, 19
Caleb M., Flynn C., Bailes M., Barr E. D., Hunstead R. W., Keane E. F., Ravi V., van Straten W., 2016, MNRAS, 458, 708
Chatterjee S. et al., 2017, Nature, 541, 58
CHIME/FRB Collaboration, 2018, ApJ, 863, 48
CHIME/FRB Collaboration, 2019a, Nature, 566, 230
CHIME/FRB Collaboration, 2019b, Nature, 566, 235
Cole T. W., Pilkington J. D. H., 1968, Nature, 219, 574
Colla G. et al., 1970, A&AS, 1, 281
Comoretto G. et al., 2017, J. Astron. Instrum., 6, 1641015
Connor L., 2019, MNRAS, 487, 1706
Cordes J. M., Chatterjee S., 2019, ARA&A, 57, 417
D'Amico N. et al., 1996, ApJS, 106, 611
Dolag K., Gaensler B. M., Beck A. M., Beck M. C., 2015, MNRAS, 451, 4277
Ficarra A., Grueff G., Tomassetti G., 1985, Astronomy and Astrophysics, Suppl. Ser., 59, 255
Gajjar V. et al., 2018, ApJ, 863, 2
Ghisellini G., 2017, MNRAS, 465, L30
Ghisellini G., Locatelli N., 2018, A&A, 613, A61
Hackstein S., Brüggen M., Vazza F., Gaensler B. M., Heesen V., 2019, MNRAS, 488, 4220
Hassall T. E. et al., 2012, A&A, 543, A66
Hobbs G., Lyne A. G., Kramer M., Martin C. E., Jordan C., 2004, MNRAS, 353, 1311
Hotan A. W., van Straten W., Manchester R. N., 2004, Publ. Astron. Soc. Aust., 21, 302
Inoue Y., Ioka K., 2012, Phys. Rev. D, 86, 023003
James C. W., Ekers R. D., Macquart J. P., Bannister K. W., Shannon R. M., 2019, MNRAS, 483, 1342
Keane E. F., 2018, Nat. Astron., 2, 865
Kocz J. et al., 2019, MNRAS, 489, 919
Kumar P. et al., 2019, ApJ, 887, L30
Locatelli N., Ronchi M., Ghirlanda G., Ghisellini G., 2019, A&A, 625, A109
Lorimer D. R., 2011, Astrophysics Source Code Library, record ascl:1107.016
Lorimer D. R., Yates J. A., Lyne A. G., Gould D. M., 1995, MNRAS, 273, 411
Lorimer D. R., Bailes M., McLaughlin M. A., Narkevic D. J., Crawford F., 2007, Science, 318, 777
Lyutikov M., 2017, ApJ, 838, L13
Macquart J.-P., 2018, Nat. Astron., 2, 836
Macquart J. P., Ekers R., 2018, MNRAS, 480, 4211
Macquart J. P., Shannon R. M., Bannister K. W., James C. W., Ekers R. D., Bunton J. D., 2019, ApJ, 872, L19
Madau P., Dickinson M., 2014, ARA&A, 52, 415
Magro A., et al., 2017, 2017 International Conference on Signals and Systems (ICSigSys), p. 190
Magro A., Bugeja K., Chiello R., DeMarco A., 2019, 2019 IEEE-APS Topical Conference on Antennas and Propagation in Wireless Communications (APWC), p. 069
McQuinn M., 2014, ApJ, 780, L33
Michilli D. et al., 2018, Nature, 553, 182
Montebugnoli S., Bianchi G., Monari J., Naldi G., Perini F., Schiaffino M., 2009, Proc. Sci., BEST: Basic Element for SKA Training. SISSA, Trieste, PoS#58
Naldi G. et al., 2017, J. Astron. Instrum., 06
Niino Y., 2018, ApJ, 858, 4
Patel C. et al., 2018, ApJ, 869, 181
Pedani M., Grueff G., 1999, A&A, 350, 368
Pedregosa F. et al., 2012, preprint (arXiv:1201.0490)
Perini F., 2009a, Proc. Sci., Low Noise Design Experience for the SKADS/BEST Demonstrator. SISSA, Trieste, PoS#60
Perini F., 2009b, Proc. Sci., Analogue Optical Links Experiences in the Framework of the SKA/BEST Activities. SISSA, Trieste, PoS#61
Perini F., Bianchi G., Schiaffino M., Monari J., 2009, Proc. Sci., BEST Receiver Experience: General Architecture, Design and Integration. SISSA, Trieste, PoS#62
Perley R. A., Butler B. J., 2017, ApJS, 230, 7
Petroff E. et al., 2015, MNRAS, 447, 246
Petroff E., Hessels J. W. T., Lorimer D. R., 2019, A&AR, 27, 4
Platts E., Weltman A., Walters A., Tendulkar S. P., Gordin J. E. B., Kandhai S., 2019, Physics Reports, 821, 1
Ransom S. M., 2001, PhD thesis, Harvard University
Ransom S. M., Eikenberry S. S., Middleditch J., 2002, AJ, 124, 1788
Ravi V., 2019, ApJ, 872, 88
Ravi V. et al., 2019, Nature, 572, 352
Sanidas S. et al., 2019, A&A, 626, A104
Shannon R. M. et al., 2018, Nature, 562, 386
Sokolowski M. et al., 2018, ApJ, 867, L12
Spitler L. G. et al., 2014, ApJ, 790, 101
Spitler L. G. et al., 2016, Nature, 531, 202
ter Veen S. et al., 2019, A&A, 621, A57
The CHIME/FRB Collaboration, 2019, ApJ, 885, L24
Thornton D. et al., 2013, Sci, 341, 53
van Straten W., Bailes M., 2011, Publ. Astron. Soc. Aust., 28, 1
Vazza F., Brüggen M., Gheller C., Hackstein S., Wittor D., Hinz P. M., 2017, Class. Quantum Gravity, 34, 234001
Vazza F., Brüggen M., Hinz P. M., Wittor D., Locatelli N., Gheller C., 2018, MNRAS, 480, 3907
Vedantham H. K., Ravi V., Hallinan G., Shannon R. M., 2016, ApJ, 830, 75
Zhang G. Q., Wang F. Y., 2019, MNRAS, 487, 3672

This paper has been typeset from a TEX/LATEX file prepared by the author.

---

[3] http://www.astropy.org